Dieses Dokument ist eine Zweitveröffentlichung (Postprint) /

This is a self-archiving document (accepted version):

Michael Hoffmann, Franz P. G. Fengler, Melanie Herzig, Terence Mittmann, Benjamin Max, Uwe Schroeder, Raluca Negrea, Pinitilie Lucian, Stefan Slesazeck, Thomas Mikolajick

# Unveiling the double-well energy landscape in a ferroelectric layer

**Erstveröffentlichung in / First published in:**

*Nature.* 2019, 565, S. 464-467 [Zugriff am: 17.10.2022]. Springer Nature. ISSN 1476-4687.

DOI: https://doi.org/10.1038/s41586-018-0854-z

Diese Version ist verfügbar / This version is available on:

https://nbn-resolving.org/urn:nbn:de:bsz:14-qucosa2-815183

SLUB
Wir führen Wissen.

TECHNISCHE UNIVERSITÄT DRESDEN

QUCOSA Quality Content of Saxony

Final edited form was published in "Nature". 2019, 565, S. 464-467. ISSN 1476-4687.
https://doi.org/10.1038/s41586-018-0854-z

# Unveiling the double-well energy landscape in a ferroelectric layer

Michael Hoffmann[1]*, Franz P. G. Fengler[1], Melanie Herzig[1], Terence Mittmann[1], Benjamin Max[2], Uwe Schroeder[1], Raluca Negrea[3], Pintilie Lucian[3], Stefan Slesazeck[1] & Thomas Mikolajick[1,2]

[1]NaMLab, Dresden, Germany.
[2]Institute of Semiconductors and Microsystems, TU Dresden, Dresden, Germany.
[3]National Institute of Materials Physics, Magurele, Romania.
*e-mail: michael.hoffmann@namlab.com

**The properties of ferroelectric materials, which were discovered almost a century ago[1], have led to a huge range of applications, such as digital information storage[2], pyroelectric energy conversion[3] and neuromorphic computing[4,5]. Recently, it was shown that ferroelectrics can have negative capacitance[6–11], which could improve the energy efficiency of conventional electronics beyond fundamental limits[12–14]. In Landau–Ginzburg–Devonshire theory[15–17], this negative capacitance is directly related to the double-well shape of the ferroelectric polarization–energy landscape, which was thought for more than 70 years to be inaccessible to experiments[18]. Here we report electrical measurements of the intrinsic double-well energy landscape in a thin layer of ferroelectric $Hf_{0.5}Zr_{0.5}O_2$. To achieve this, we integrated the ferroelectric into a heterostructure capacitor with a second dielectric layer to prevent immediate screening of polarization charges during switching. These results show that negative capacitance has its origin in the energy barrier in a double-well landscape. Furthermore, we demonstrate that ferroelectric negative capacitance can be fast and hysteresis-free, which is important for prospective applications[19]. In addition, the $Hf_{0.5}Zr_{0.5}O_2$ used in this work is currently the most industry-relevant ferroelectric material, because both $HfO_2$ and $ZrO_2$ thin films are already used in everyday electronics[20]. This could lead to fast adoption of negative capacitance effects in future products with markedly improved energy efficiency.**

Since the 1940s, phenomena in ferroelectric materials have been successfully modelled on the basis of the Landau theory of phase transitions[15], which was first applied to ferroelectrics by Ginzburg and Devonshire[16,17]. Phenomenological models based on this Landau–Ginzburg–Devonshire (LGD) approach have been an essential tool in understanding the basic physics of ferroelectricity[18]. In LGD theory, a ferroelectric below its transition temperature is described by a double-well free energy landscape $F$ as a function of the polarization $P$ as shown in Fig. 1a; here $F$ is the Helmholtz free energy density. The two degenerate energy minima define two stable spontaneous polarization states, $\pm P_S$, in the material, which can be reversed by the application of an electric field. By differentiating $F$ with respect to $P$, one obtains the 'S'-shaped $P$–$E_F$ characteristics depicted in Fig. 1b, where $E_F$ is the electric field in the ferroelectric. This 'S'-shape of the $P$–$E_F$ curve implies that in a certain region around $P \approx 0$ the ferroelectric possesses a differential negative capacitance, because the capacitance $C$ is proportional to the slope[12] $dP/dE_F$, which is a direct consequence of the energy barrier in Fig. 1a[6,21]. This means that the double-well energy landscape could be reconstructed from an electrical measurement of the 'S'-shaped $P$–$E_F$ curve by a simple integration with respect to $P$. However, the negative capacitance region of the 'S'-shaped $P$–$E_F$ curve is not easily observed in ferroelectrics because of its unstable nature, as it corresponds to an energy maximum of $F$. Only recently, several groups have experimentally demonstrated negative capacitance effects in ferroelectrics[6–11]. Nevertheless, an experimental 'S'-shaped $P$–$E_F$ curve, as in Fig. 1b, has not been reported. Indeed, the prevailing opinion is that such an 'S'-shaped $P$–$E_F$ curve cannot be measured in ferroelectric materials owing to the formation of domains or an immediate screening of the polarization by free charges[22].

In the following, we describe a way to extract the 'S'-shaped $P$–$E_F$ curve of a ferroelectric layer using electrical measurements, which enable a reconstruction of the double-well energy landscape. Furthermore, we demonstrate this method for ferroelectric $Hf_{0.5}Zr_{0.5}O_2$ (HZO) thin films, which are most promising for practical applications because they are lead-free, highly scalable and fully compatible with current semiconductor manufacturing techniques[20].

First, we fabricated and characterized metal–ferroelectric–metal (MFM) capacitors to confirm ferroelectricity in the thin (11.6-nm) HZO films used, as described in detail in Methods. Figure 2a shows a typical ferroelectric $P$–$E_F$ hysteresis loop with a remanent polarization $P_r$ of about 17 μC cm$^{-2}$ and a coercive field $E_c$ of about 1.2 MV cm$^{-1}$, which is in agreement with reports from literature[20]. Grazing-incidence X-ray diffraction (GIXRD) patterns of the polycrystalline HZO films, shown in Fig. 2b, confirm a mixture of the paraelectric tetragonal phase and the ferroelectric orthorhombic phase, with only a small fraction of the monoclinic phase (see reference patterns for $HfO_2$ in Fig. 2d). The typical 'butterfly' capacitance–voltage hysteresis shown in Fig. 2c additionally confirms ferroelectric properties of the HZO layer.

When comparing the experimental $P$–$E_F$ curve in Fig. 2a to the theoretical one in Fig. 1b, it is apparent that negative capacitance behaviour cannot be observed in standard $P$–$E_F$ hysteresis measurements. In such measurements, the voltage is forced and therefore a negative slope $dP/dE_F$ would only be reflected as a very steep incline of the polarization rather than an 'S'-shaped curve. Moreover, the screening of the polarization through the metal electrodes is much faster than the characteristic measurement time (about 0.1 ms)[22,23]. To allow for the additional voltage drop in the region of negative $dP/dE_F$ in the ferroelectric,

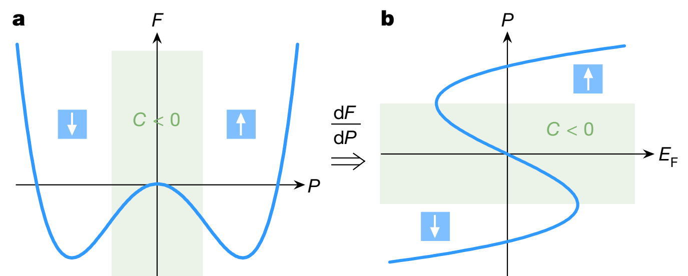


**Fig. 1 | Landau–Ginzburg–Devonshire phenomenological model of a ferroelectric. a**, Double-well landscape of the free energy $F$ in a ferroelectric as a function of the electric polarization $P$. Green shading in **a** and **b** denotes regions of negative capacitance ($C < 0$). **b**, Ferroelectric polarization–electric field ($P$–$E_F$) dependence derived from the free energy $F$. The 'S'-shaped $P$–$E_F$ curve exhibits a region of negative capacitance related to the energy barrier of $F$ in **a**. Arrows indicate ferroelectric polarization directions.



Provided by Sächsische Landesbibliothek - Staats- und Universitätsbibliothek Dresden

Final edited form was published in "Nature". 2019, 565, S. 464-467. ISSN 1476-4687.
https://doi.org/10.1038/s41586-018-0854-z

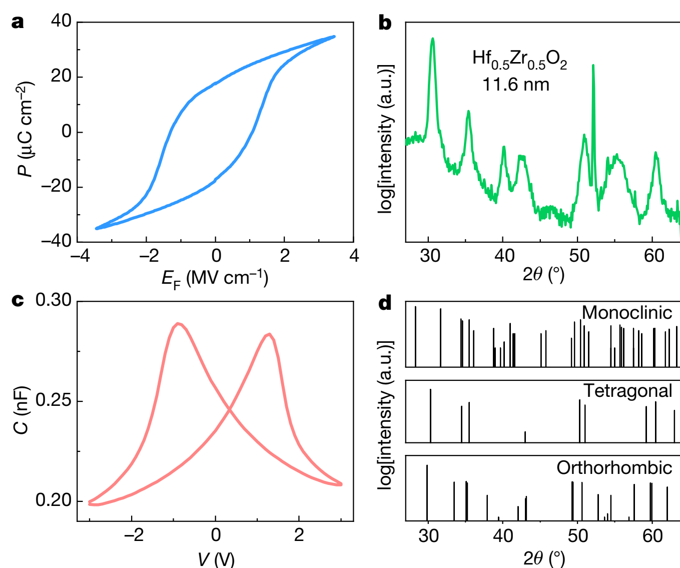


**Fig. 2 | Electrical and physical characterization of a ferroelectric $Hf_{0.5}Zr_{0.5}O_2$ layer. a**, Ferroelectric polarization–electric field ($P$–$E_F$) hysteresis of a TiN/$Hf_{0.5}Zr_{0.5}O_2$/TiN capacitor measured by applying a 10-kHz triangular voltage waveform. **b**, Grazing-incidence X-ray diffraction (GIXRD) pattern of the $Hf_{0.5}Zr_{0.5}O_2$ layer on Si. a.u., arbitrary units; $2\theta$ is the angle between the incident X-rays and the detector. **c**, Small-signal capacitance–voltage ($C$–$V$) characteristics measured at 10 kHz on the same TiN/$Hf_{0.5}Zr_{0.5}O_2$/TiN capacitor as in **a**. **d**, Reference diffraction patterns for the monoclinic, tetragonal and orthorhombic phases in $HfO_2$.

the addition of a resistor or dielectric capacitor connected in series is required for the experimental observation of the negative capacitance region in transient measurements[6,13,22]. However, such series elements can only slow down the process of supplying screening charges temporarily. Therefore, the ferroelectric will still switch during the measurement, which leads to a hysteresis in the $P$–$E_F$ curve. This can also be observed in our direct negative capacitance measurements of the MFM capacitor (shown in Fig. 2) with a resistor in series, which are presented in Extended Data Figs. 1 and 2 (see also Methods). Although the slope $dP/dE_F$ is indeed negative for a short time during switching, as shown in Extended Data Fig. 2, large hysteresis due to ferroelectric switching is still present. However, it has been proposed that the addition of a dielectric layer in direct contact with the ferroelectric could mitigate the immediate screening of the polarization charge by free charge carriers, thus leading to the temporary observation of the fundamentally unstable negative capacitance region without hysteresis[23]. In such a metal–ferroelectric–insulator–metal (MFIM) heterostructure, it is still important to measure sufficiently fast that no charges are injected into the ferroelectric/dielectric interface, which would again result in hysteretic switching due to the screening of the polarization charge[23,24]. Another concern is electrical breakdown of the dielectric layer when applying high electric fields for a prolonged time. Therefore, pulsed charge–voltage measurements are mandatory. The corresponding electrical measurement set-up is shown in Fig. 3a.

To obtain the 'S'-shaped $P$–$E_F$ curves, we fabricated MFIM capacitors with a ferroelectric HZO layer grown in the same way as the one in the MFM capacitor in Fig. 2. $Ta_2O_5$ was used as the insulating layer. Figure 3b shows a transmission electron microscopy (TEM) image of the fabricated structure to confirm the film thickness of the individual layers. The selected-area electron diffraction (SAED) patterns of the structure in Fig. 3c confirm that the HZO layer is polycrystalline, with fractions of the ferroelectric orthorhombic phase as well as the paraelectric monoclinic phase. Both TEM and SAED patterns prove the $Ta_2O_5$ layer to be amorphous. Higher resolution TEM and electron energy loss spectroscopy (EELS) data can be found in Extended Data Figs. 3 and 4. A pulse generator and an oscilloscope were connected to the MFIM capacitor (as described in Methods) to apply voltage pulses $V$, while at the same time measuring the current $I$. By integrating this current over time, the charge on the capacitor was calculated.

Short voltage pulses (width <500 ns) with increasing amplitude, as shown in Fig. 3d, were applied to the capacitor. The measured current and integrated charge as a function of time are presented in Fig. 3e and f, respectively. From the charge transients in Fig. 3f, three important charges are extracted for each voltage pulse: the maximum stored charge on the capacitor, $Q_{max}$; the residual charge on the capacitor after the applied voltage is zero again, $Q_{res}$; and the difference between $Q_{max}$ and $Q_{res}$, which is the charge $Q_{rev}$ that is reversibly stored and released from the capacitor. $Q_{rev}$ is important for applications, because it determines the effective capacitance of the layer[23]. All three charges—$Q_{max}$, $Q_{res}$ and $Q_{rev}$—are shown in Fig. 3g as a function of the voltage across the capacitor, $V_{max}$ (see Supplementary Information). Up to a pulse height of about 5 V, the slope of the $Q_{rev}$–$V_{max}$ curve, $dQ_{rev}/dV_{max}$ (which corresponds to the capacitance $C$), is roughly constant. For greater pulse heights, the slope and therefore the capacitance increases. Because the capacitance of the dielectric $Ta_2O_5$ layer should be independent of the applied voltage, this increase of the total capacitance of the MFIM heterostructure seems to originate from the HZO layer.

Under the assumption that the capacitance of the $Ta_2O_5$ layer is constant (which was determined on separate TiN/$Ta_2O_5$/TiN capacitors), we can calculate the electric field in the ferroelectric layer as well as the $P$–$E_F$ relationship shown in Fig. 3h (see Supplementary Information for details). This experimental $P$–$E_F$ curve exhibits the distinct 'S'-shape predicted by LGD theory. Indeed, the measurement results can be well fitted with a simple LGD model, as described in Supplementary Information and shown in Extended Data Fig. 5. The calculated electric fields inside the layers are shown in Extended Data Fig. 5b and c for HZO and $Ta_2O_5$, respectively. One can see that for HZO, the external field $E_{F,ext}$ and the depolarization field $E_{dep}$ largely compensate each other, leading to only moderate total fields $E_F$. In contrast, for the $Ta_2O_5$ layer, the internal field $E_{D,int}$ and the external field $E_{D,ext}$ have the same sign, leading to very high total electric fields $E_D$. Therefore, the application of higher voltages was limited by dielectric breakdown of the $Ta_2O_5$ layer.

The measured 'S'-shaped characteristics indicate that the ferroelectric is initially in the negative remanent polarization state ($P_r$ is about 15.5 μC cm$^{-2}$, which is very close to the value shown in Fig. 2a for the MFM sample). Then, during application of the positive voltage pulse, the ferroelectric enters a region of negative capacitance, since the polarization charge is temporarily unscreened at the ferroelectric/dielectric interface[23]. No hysteretic switching is observed, because not enough free charges can tunnel to the interface to compensate the ferroelectric polarization[22,23]. However, there must be some fixed charge $\sigma_{IF}$ at this interface initially, which reduces the depolarization field to zero when no voltage is applied (no negative reset pulse was needed), see equation (4) in Supplementary Information and Extended Data Fig. 5b. Without $\sigma_{IF}$, the unscreened spontaneous polarization at the ferroelectric/dielectric interface would lead to a large depolarization field, which in turn would lead to domain formation[10,21] and thus preclude the observation of the 'S'-shaped $P$–$E_F$ curve and double-well energy landscape. For the highest applied voltages, the ferroelectric is in a positive capacitance state again, which, however, is not stable when removing the applied voltage, since only the negative remanent polarization charge is screened by the fixed charge $\sigma_{IF}$ at the ferroelectric/dielectric interface. The ferroelectric layer was always in the negative remanent state after the voltage was reduced to zero in these experiments.

From the experimental 'S'-shaped $P$–$E_F$ curve in Fig. 3h, we can now calculate the free energy by integration with respect to $P$ (see Supplementary Information for details). The calculated free energy as a function of $P$ is shown in Fig. 3i. The clear shape of a double-well potential can be seen, even if one cannot measure the second energy minimum completely owing to the limitation of dielectric breakdown. The same LGD model from Fig. 3h was also added to Fig. 3i, demonstrating an excellent agreement with the experimental data. To confirm that there is no hysteretic switching during the measurement, ascending


Provided by Sächsische Landesbibliothek - Staats- und Universitätsbibliothek Dresden

Final edited form was published in "Nature". 2019, 565, S. 464-467. ISSN 1476-4687.
https://doi.org/10.1038/s41586-018-0854-z

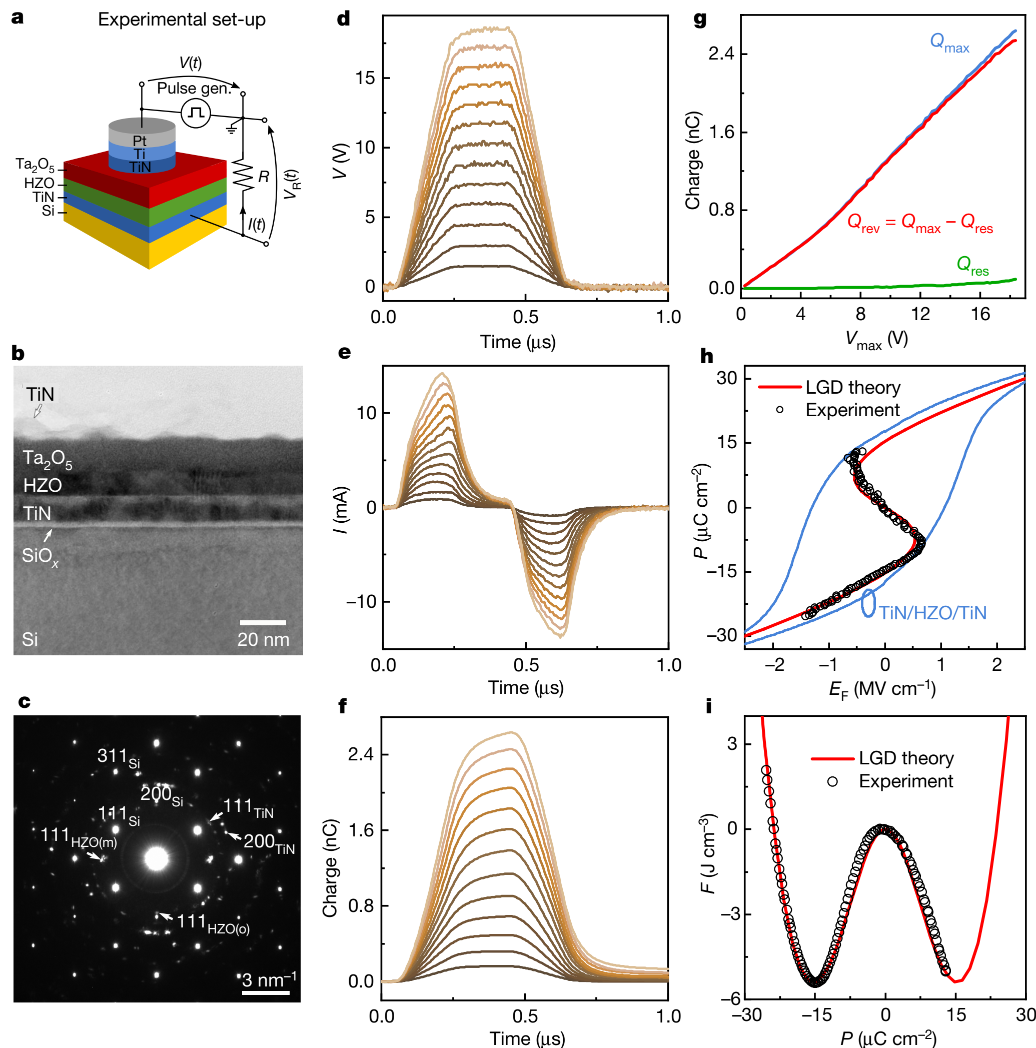


**Fig. 3 | Electrical measurement of the ferroelectric double-well energy landscape.** **a**, Schematic experimental set-up for the pulsed charge–voltage measurements on circular capacitor pads. Voltage $V$ is applied by a pulse generator (pulse gen.), and both $V$ and $V_R$ are measured via an oscilloscope, where $V_R$ is the voltage drop across the resistance $R$. **b**, Transmission electron microscopy (TEM) image of the ferroelectric/dielectric TiN/$Ta_2O_5$/$Hf_{0.5}Zr_{0.5}O_2$/TiN heterostructure capacitor. **c**, Selected-area electron diffraction (SAED) pattern of the heterostructure shown in **b**. TEM and the SAED pattern confirm a mixture of orthorhombic and monoclinic grains in the $Hf_{0.5}Zr_{0.5}O_2$ layer and the amorphous nature of the $Ta_2O_5$ layer. **d**–**f**, The applied voltage pulses, the measured current response and the integrated charge, respectively, as a function of time. **g**, The maximum charge $Q_{max}$ and residual charge $Q_{res}$, together with their difference, $Q_{rev} = Q_{max} - Q_{res}$; these are derived from **f** as a function of the voltage across the capacitor ($V_{max}$) in **d**. **h**, The calculated polarization–electric field relationship of the $Hf_{0.5}Zr_{0.5}O_2$ layer with a fit according to LGD theory. **i**, The result of integrating the $P$–$E_F$ characteristics in **h**. As a result, the double-well energy landscape is obtained from experimental data. The fit in **i** uses the same LGD coefficients as in **h**.

and descending voltage pulses were applied in sequence. Extended Data Fig. 6a and b prove that there is indeed negligible hysteresis. Furthermore, to exclude the possibility that the reported behaviour is only caused by the properties of the $Ta_2O_5$ layer and to investigate the scalability of the effect, similar experiments were carried out on samples using a thin (4 nm) $Al_2O_3$ layer as a dielectric and a thin (7.7 nm) ferroelectric HZO layer. As shown in Extended Data Fig. 6c and d, a similar negative capacitance region can be observed, which can again be understood as originating from the barrier in the double-well energy landscape.

Although the experimental negative capacitance effects reported here are transient and not stabilized[21,22], they are still of interest for applications since there is no hysteresis and the effects seem to be very fast (only limited by our measurement set-up and capacitor size)[23]. Our findings could be used to create more energy-efficient dynamic random access memories[23], because less voltage would be needed to store the same amount of charge while at the same time resulting in lower leakage currents due to the increased overall layer thickness. Furthermore, integrating a ferroelectric layer into the gate-stack of a field-effect transistor could be used to reduce the voltage needed to change the drain current by one order of magnitude below the fundamental Boltzmann limit of 60 mV per decade at room temperature[12]. This would lead to much more energy-efficient integrated circuits by allowing a further reduction of the operating voltage. Indeed, recent results[25] on integrated transistors in a 14-nm technology showed that devices with a ferroelectric in the gate stack could operate more efficiently than reference devices at frequencies up to 40 GHz. For such applications in digital electronics, the transient nature of the negative capacitance effect shown here should not be a concern, since these devices rely on pulsed voltage operation similar to that demonstrated in our experiments. In general, stabilization of a single-domain negative capacitance state in ferroelectrics is still elusive, since depolarization fields will typically favour multi-domain formation to reduce the depolarization energy[21,26]. However, Zubko et al.[10] showed that even a ferroelectric in a complex multi-domain state can give rise to stabilized negative capacitance effects. On the other hand, our results show that fixed charges at the ferroelectric/dielectric interface can help to stabilize the single-domain state and thus enable the transient observation


Provided by Sächsische Landesbibliothek - Staats- und Universitätsbibliothek Dresden

of the intrinsic negative capacitance region without the ferroelectric breaking into domains.

The results reported here will also help in the development of more accurate ferroelectric models based on LGD theory and pulsed electrical measurements. Furthermore, our results present a unique look into the intrinsic energy landscape of ferroelectric materials, which could pave the way towards new applications in information processing, sensing or energy conversion and will shed new light on connecting experimental results to fundamental ferroelectric theory.

## Online content

Any methods, additional references, Nature Research reporting summaries, source data, statements of data availability and associated accession codes are available at https://doi.org/10.1038/s41586-018-0854-z.


1. Valasek, J. *Piezo-electric and Allied Phenomena in Rochelle Salt*. MSc thesis, Univ. Minnesota (1920).
2. Buck, D. A. *Ferroelectrics for Digital Information Storage and Switching*. MSc thesis, MIT (Report R-212, 1952).
3. Pandya, S. et al. Pyroelectric energy conversion with large energy and power density in relaxor ferroelectric thin films. *Nat. Mater*. **17**, 432–438 (2018).
4. Chanthbouala, A. et al. A ferroelectric memristor. *Nat. Mater*. **11**, 860–864 (2012).
5. Mulaosmanovic, H. et al. Novel ferroelectric FET based synapse for neuromorphic systems. In *2017 Symposium on VLSI Technology* T176–T177 (2017).
6. Khan, A. I. et al. Negative capacitance in a ferroelectric capacitor. *Nat. Mater*. **14**, 182–186 (2015).
7. Khan, A. I. et al. Experimental evidence of ferroelectric negative capacitance in nanoscale heterostructures. *Appl. Phys. Lett.* **99**, 113501 (2011).
8. Appleby, D. J. R. et al. Experimental observation of negative capacitance in ferroelectrics at room temperature. *Nano Lett.* **14**, 3864–3868 (2014).
9. Gao, W. et al. Room-temperature negative capacitance in a ferroelectric–dielectric superlattice heterostructure. *Nano Lett.* **14**, 5814–5819 (2014).
10. Zubko, P. et al. Negative capacitance in multidomain ferroelectric superlattices. *Nature* **534**, 524–528 (2016).
11. Hoffmann, M. et al. Direct observation of negative capacitance in polycrystalline ferroelectric $HfO_2$. *Adv. Funct. Mater*. **26**, 8643–8649 (2016).
12. Salahuddin, S. & Datta, S. Use of negative capacitance to provide voltage amplification for low power nanoscale devices. *Nano Lett.* **8**, 405–410 (2008).
13. Khan, A. I. et al. Differential voltage amplification from ferroelectric negative capacitance. *Appl. Phys. Lett.* **111**, 253501 (2017); erratum **112**, 089901 (2018).
14. Wong, J. C. & Salahuddin, S. Breaking the fundamental energy dissipation limit in ferroelectric-dielectric capacitors. Preprint at https://arxiv.org/abs/1805.04259 (2018).
15. Landau, L. D. On the theory of phase transitions. *Zh. Eksp. Teor. Fiz.* **7**, 19–32 (1937).
16. Ginzburg, V. L. On the dielectric properties of ferroelectric (Segnette-electric) crystals and barium titanate. *Zh. Eksp. Teor. Fiz.* **15**, 739–749 (1945).
17. Devonshire, A. F. XCVI. Theory of barium titanate. Part I. *Phil. Mag.* **40**, 1040–1063 (1949).
18. Landau, L. D. & Lifshitz, E. M. *Electrodynamics of Continuous Media* (Pergamon, Oxford, 1960).
19. Si, M. et al. Steep-slope hysteresis-free negative capacitance $MoS_2$ transistors. *Nat. Nanotechnol*. **13**, 24–28 (2018).
20. Müller, J. et al. Ferroelectricity in simple binary $ZrO_2$ and $HfO_2$. *Nano Lett.* **12**, 4318–4323 (2012).
21. Hoffmann, M., Pešić, M., Slesazeck, S., Schroeder, U. & Mikolajick, T. On the stabilization of ferroelectric negative capacitance in nanoscale devices. *Nanoscale* **10**, 10891–10899 (2018).
22. Hoffmann, M. et al. Ferroelectric negative capacitance domain dynamics. *J. Appl. Phys*. **123**, 184101 (2018).
23. Kim, Y. J. et al. Time-dependent negative capacitance effects in $Al_2O_3/BaTiO_3$ bilayers. *Nano Lett.* **16**, 4375–4381 (2016).
24. Kim, Y. J. et al. Frustration of negative capacitance in $Al_2O_3/BaTiO_3$ bilayer structure. *Sci. Rep*. **6**, 19039 (2016).
25. Krivokapic, Z. et al. 14nm ferroelectric FinFET technology with steep subthreshold slope for ultra low power applications. In *2017 IEEE International Electron Devices Meeting (IEDM)* 357–360 (2017).
26. Cano, A. & Jiménez, D. Multidomain ferroelectricity as a limiting factor for voltage amplification in ferroelectric field-effect transistors. *Appl. Phys. Lett.* **97**, 133509 (2010).


**Acknowledgements** This project received funding from the Electronic Component Systems for European Leadership Joint Undertaking under grant agreement no. 692519. This Joint Undertaking receives support from the European Union's Horizon 2020 research and innovation programme and Belgium, Germany, France, Netherlands, Poland and the UK. This work was also supported in part by the EFRE fund of the European Commission and in part by the Free State of Saxony (Germany). P.L. and R.N. acknowledge funding through the Core Program of NIMP (Romanian Ministry for Research and Innovation).

**Reviewer information** *Nature* thanks D. Jiménez, A. Morozovska and L.-E. Wernersson for their contribution to the peer review of this work.

**Author contributions** M. Hoffmann performed the electrical measurements, analysed the data and wrote the manuscript. F.P.G.F., M. Herzig and B.M. fabricated the samples. T. Mittmann optimized the HZO atomic layer deposition process. P.L. and R.N. performed TEM measurements and analyses. U.S., S.S. and T. Mikolajick supervised the work and discussed the results. S.S. and M. Hoffmann conceived and designed the experiments. All authors commented on the manuscript.

**Competing interests** The authors declare no competing interests.

**Additional information**
**Extended data** is available for this paper at https://doi.org/10.1038/s41586-018-0854-z.
**Supplementary information** is available for this paper at https://doi.org/10.1038/s41586-018-0854-z.
**Reprints and permissions information** is available at http://www.nature.com/reprints.
**Correspondence and requests for materials** should be addressed to M.H.
**Publisher's note:** Springer Nature remains neutral with regard to jurisdictional claims in published maps and institutional affiliations.


Provided by Sächsische Landesbibliothek - Staats- und Universitätsbibliothek Dresden

Final edited form was published in "Nature". 2019, 565, S. 464-467. ISSN 1476-4687.
https://doi.org/10.1038/s41586-018-0854-z

# METHODS

**Sample fabrication.** Metal–ferroelectric–metal (MFM) and metal–ferroelectric–insulator–metal (MFIM) capacitors were fabricated on Si(100) substrates with a native $SiO_2$ layer. Bottom TiN electrodes of 12-nm thickness were reactively sputtered in a BESTEC and an Alliance Concept physical vapour deposition tool at room temperature. Subsequently, $Hf_{0.5}Zr_{0.5}O_2$ (HZO) films were grown by atomic layer deposition (ALD) in an Oxford Instruments OpAL ALD tool at 260 °C using the precursors TEMA-Hf and TEMA-Zr, with water as the oxygen source. Alternating ALD cycles of TEMA-Hf and TEMA-Zr were applied to achieve a homogeneous distribution of Hf and Zr in the films. For MFIM samples using $Al_2O_3$, ALD was carried out directly after HZO deposition without breaking vacuum using TMA and water as precursors at 260 °C. The film thicknesses were adjusted by the total number of ALD cycles. On the other hand, MFIM samples with $Ta_2O_5$ were fabricated by reactive sputtering of $Ta_2O_5$ at room temperature after ALD of HZO. Top TiN electrodes were then deposited in the same way as the bottom electrodes. After top electrode deposition, crystallization of the HZO layers was achieved by annealing the samples at 500 °C and 600 °C for 20 s in nitrogen atmosphere for $Ta_2O_5$ and $Al_2O_3$ samples, respectively. To define circular capacitor areas ($A \approx 8{,}000\ \mu m^2$), 10-nm Ti and 50-nm Pt were evaporated through a shadow mask. These evaporated Pt dots served as a hard mask during the subsequent wet etch ($NH_4OH$ and $H_2O_2$ in $H_2O$ solution) of the TiN top electrode. Reference capacitors of TiN/$Ta_2O_5$/TiN and TiN/$Al_2O_3$/TiN were fabricated in the same way as described above, just omitting the HZO ALD step, to obtain the permittivity of $Ta_2O_5$ and $Al_2O_3$.

**Characterization.** X-ray reflectometry (XRR) and grazing-incidence X-ray diffraction (GIXRD) measurements were carried out on a Bruker D8 Discover (Cu-K$\alpha$ radiation, $\lambda = 0.154$ nm) for structural analysis of the samples. The microstructural investigations of the MFIM specimens containing $Ta_2O_5$ were performed by Transmission Analytical Electron Microscopy using a JEM ARM 200F High Resolution Electron Microscope operated at 200 kV and equipped with Gatan Quantum SE for Electron Energy Loss Spectroscopy (EELS) measurements. The samples were analysed in the microscope in conventional (diffraction contrast imaging) and high-resolution modes, with fixed and parallel beam (TEM/HRTEM) and scanning (STEM) with convergent beam. The chemical composition was investigated using the electron microscope in the EELS analytical mode. Cross-section TEM specimens were prepared from the samples by mechanical polishing down to about 30 μm, followed by ion milling in a Gatan PIPS machine at 4 kV accelerating voltage and 7° incidence angle. Low-voltage (2 kV) milling was used as a final ion polishing stage to reduce the amorphous surface layer enveloping the specimen.

Electrical measurements were carried out on a Cascade Microtech RF Probe Station with a Keithley 4200 SCS with a 4225-PMU and RPM remote amplifier, an HP 8110A pulse generator and a Tektronix TDS7154B digital oscilloscope. Polarization–electric field hysteresis curves were measured by applying triangular voltage signals with 10 kHz frequency to the capacitors after previous application of $10^4$ rectangular voltage pulses at 100 kHz which was done to account for the so-called 'wake-up' effect. Capacitance voltage measurements were carried out using a small-signal amplitude of 50 mV and a frequency of 10 kHz. For pulsed charge–voltage measurements, capacitors were connected to the pulse generator while measuring the current and voltage via the oscilloscope with a 50 Ω and 1 MΩ input impedance, respectively.

**Effect of increased voltage pulse length and charge injection.** When repeating the same measurements for the HZO/$Ta_2O_5$ sample in Fig. 3 with longer voltage pulses, we observed that charge trapping increased, which led to an appearance of hysteresis while the overall capacitance enhancement due to negative capacitance in the HZO layer decreased (Extended Data Fig. 7a, b). The increase of $Q_{rev}$ for longer pulse widths is mostly related to the frequency dispersion of the $Ta_2O_5$ layer, which was considered when calculating the respective $P$–$E_F$ curves. However, we were not able to completely switch the HZO layer even for the longest pulse widths of 400 μs, since early dielectric breakdown precluded the injection of sufficient charge to the HZO/$Ta_2O_5$ interface. To further investigate the transition from hysteresis-free negative capacitance effects to hysteretic polarization switching[23], we fabricated HZO/$Al_2O_3$ capacitors with only 3-nm $Al_2O_3$ thickness. Here, increased charge injection was observed before dielectric breakdown occurred. Extended Data Fig. 7c, d show respectively $Q_{rev}$–$V_{max}$ and $P$–$E_F$ curves for this sample when successively increasing the maximum pulse amplitude (that is, 0 V → 8 V → 0 V, then 0 V → 9 V → 0 V, and so on). For the lowest maximum voltage of 8 V, hysteresis-free negative capacitance was observed. However, for higher voltages, charge injection led to increased hysteresis and successive switching of the HZO layer. For 11 V, the ferroelectric negative capacitance region vanished completely in the descending $P$–$E_F$ branch since a significant fraction of the film was switched to the positive polarization state. These results clearly show that charge trapping itself cannot explain the hysteresis-free negative capacitance effect we observe for sufficiently short pulses, which must originate from the ferroelectric HZO layer.

**Direct measurement of transient negative capacitance in an MFM capacitor.** As shown in Extended Data Figs. 1 and 2, it is possible to directly measure negative capacitance in an MFM capacitor connected in series to a resistance $R$. When applying bipolar voltage pulses $V_S$ by using a pulse generator, we can measure the voltage across the MFM capacitor $V_F$ via an oscilloscope. The current $I_R$ flowing through $R$ can be calculated as $I_R = (V_S - V_F)/R$. The charge on the MFM capacitor is then obtained by integrating the current over time. As described elsewhere[11], the ferroelectric polarization $P$ can then be calculated from the charge on the capacitor. Plotting $P$ as a function of $E_F = V_F/t_F$ then results in the $P$–$E_F$ hysteresis shown in Extended Data Fig. 2. The regions of $dP/dE_F < 0$ correspond to an effective ferroelectric negative capacitance at the onset of polarization switching. However, large hysteresis cannot be prevented in this type of measurement, since polarization screening is only temporarily slowed down but not inhibited.

## Data availability

The datasets generated and analysed during this study are available from the corresponding author upon reasonable request.



Provided by Sächsische Landesbibliothek - Staats- und Universitätsbibliothek Dresden

Final edited form was published in "Nature". 2019, 565, S. 464-467. ISSN 1476-4687.
https://doi.org/10.1038/s41586-018-0854-z

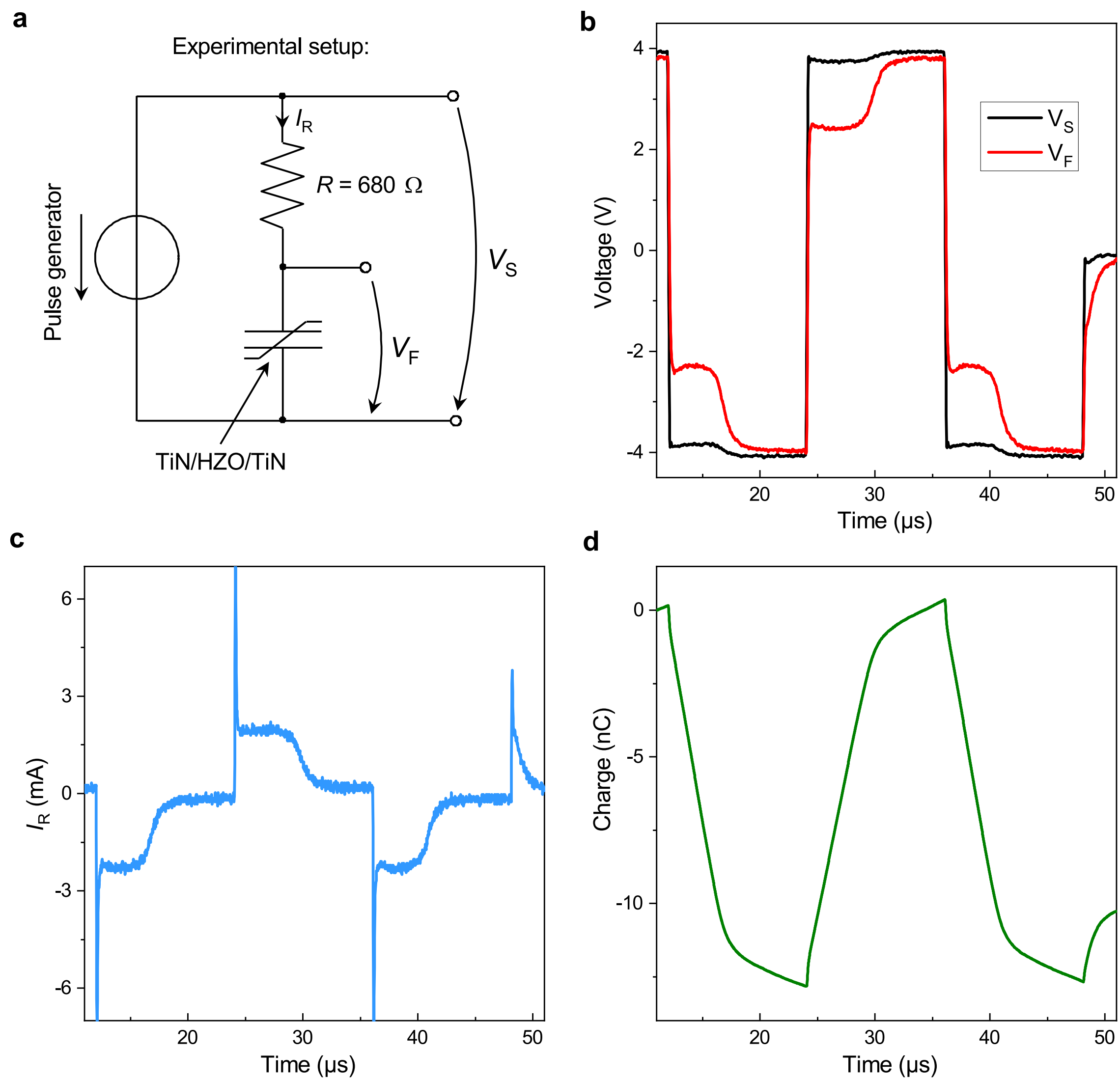


**Extended Data Fig. 1 | Direct measurement of transient negative capacitance with hysteresis in a TiN/HZO/TiN capacitor.** **a**, Experimental set-up with resistor in series. See Methods for details. **b**, Transient applied voltage ($V_S$) and ferroelectric voltage ($V_F$) measured via an oscilloscope. **c**, Calculated transient current $I_R$ flowing through the resistor $R$. **d**, Transient charge on the capacitor from integration of $I_R$.


Provided by Sächsische Landesbibliothek - Staats- und Universitätsbibliothek Dresden

Final edited form was published in "Nature". 2019, 565, S. 464-467. ISSN 1476-4687.
https://doi.org/10.1038/s41586-018-0854-z

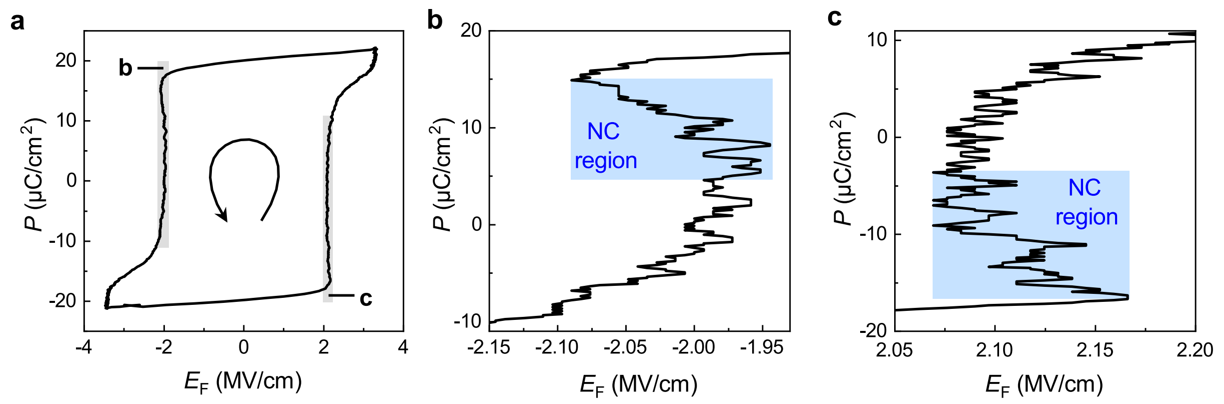


**Extended Data Fig. 2 | Ferroelectric polarization–electric field hysteresis from transient negative capacitance measurements on TiN/HZO/TiN. a**, Ferroelectric polarization–electric field ($P$–$E_F$) hysteresis calculated from the data in Extended Data Fig. 1b and d. **b**, **c**, Grey shaded areas in **a** are shown at higher magnification; the negative capacitance (NC) regions are shown with blue shading. Negative capacitance is shown for negative (**b**) and positive (**c**) electric fields.


Provided by Sächsische Landesbibliothek - Staats- und Universitätsbibliothek Dresden

Final edited form was published in "Nature". 2019, 565, S. 464-467. ISSN 1476-4687.
https://doi.org/10.1038/s41586-018-0854-z

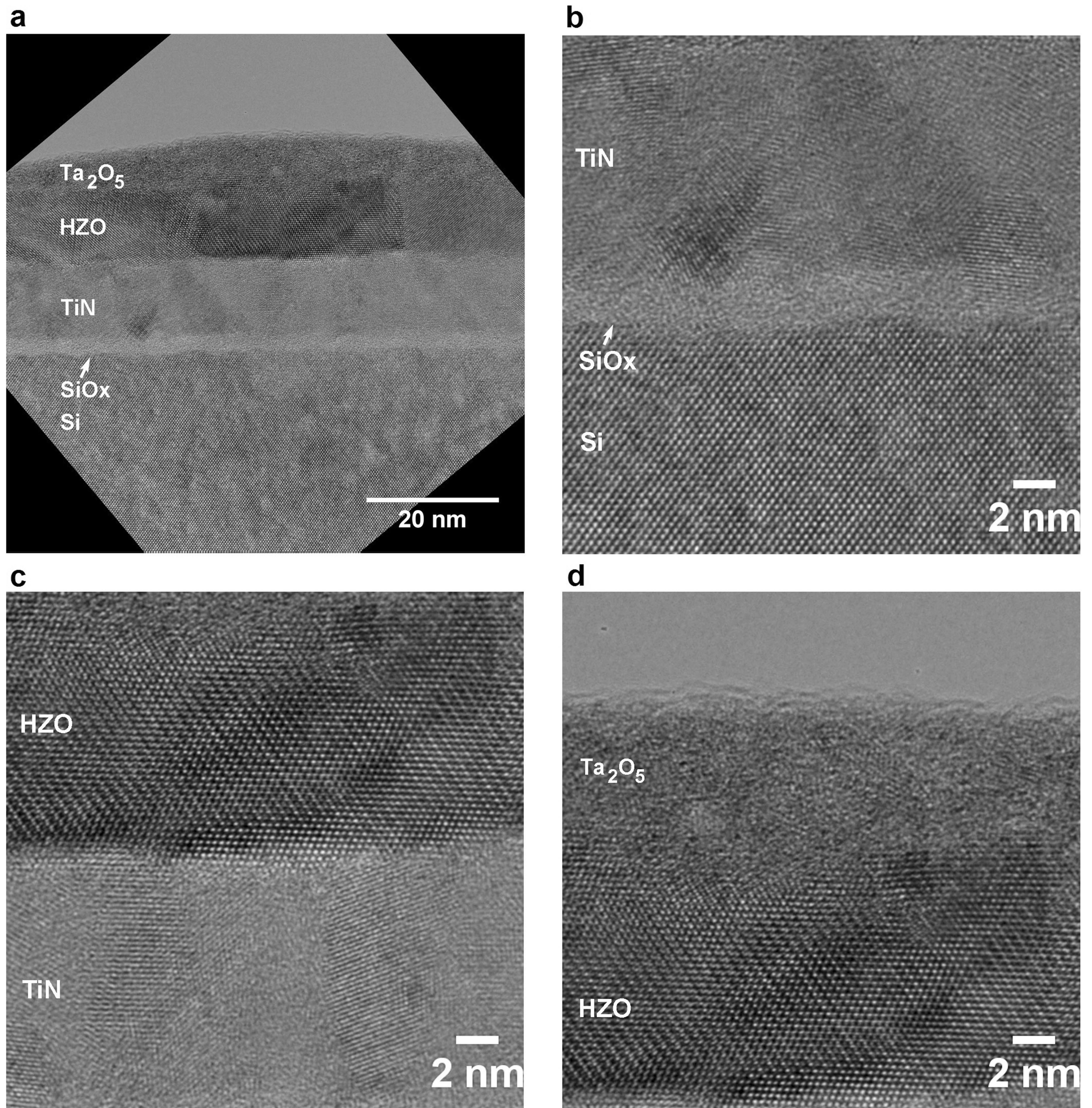


**Extended Data Fig. 3 | HRTEM images of the $Ta_2O_5$/HZO/TiN/$SiO_x$/Si heterostructure.** **a**, High-resolution transmission electron microscopy (HRTEM) images of the $Ta_2O_5$/HZO/TiN/$SiO_x$/Si heterostructure. **b**–**d**, Magnified views of particular areas of **a**: **b**, the TiN/$SiO_x$/Si interfaces; **c**, the HZO/TiN interface; and **d**, the $Ta_2O_5$/HZO interface.


Provided by Sächsische Landesbibliothek - Staats- und Universitätsbibliothek Dresden

Final edited form was published in "Nature". 2019, 565, S. 464-467. ISSN 1476-4687.
https://doi.org/10.1038/s41586-018-0854-z

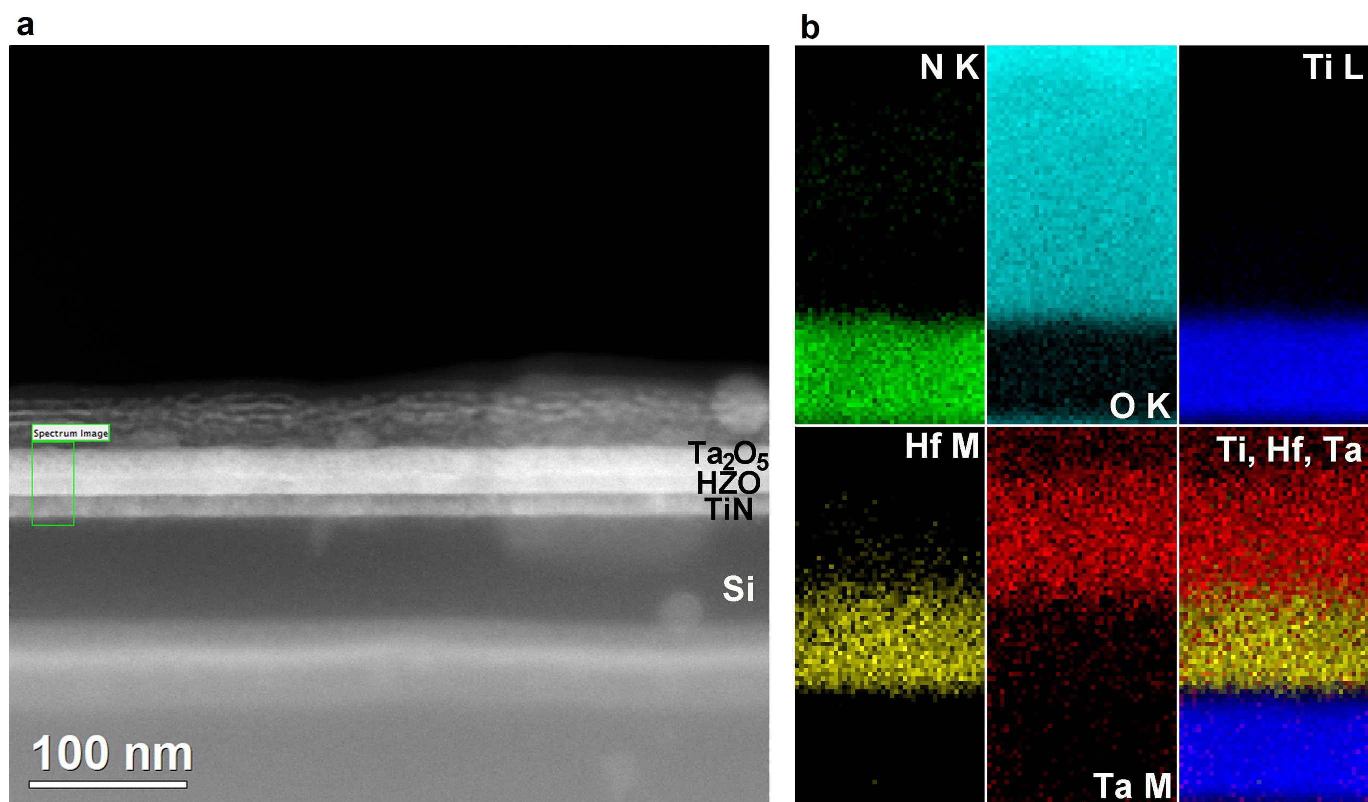


**Extended Data Fig. 4 | Heterostructure characterization by HAADF-STEM and EELS.** **a**, Low-magnification HAADF-STEM (high-angle annular dark-field scanning transmission electron microscopy) image of the $Ta_2O_5$/HZO/TiN/$SiO_x$/Si heterostructure. The boxed region was analysed by EELS (electron energy-loss spectroscopy). **b**, EELS maps corresponding to the boxed region in **a** for the absorption edges N K, O K, Ti L, Hf M and Ta M. The bottom right image was obtained by overlapping the Ti L, Hf M and Ta M maps.


Provided by Sächsische Landesbibliothek - Staats- und Universitätsbibliothek Dresden

Final edited form was published in "Nature". 2019, 565, S. 464-467. ISSN 1476-4687.
https://doi.org/10.1038/s41586-018-0854-z

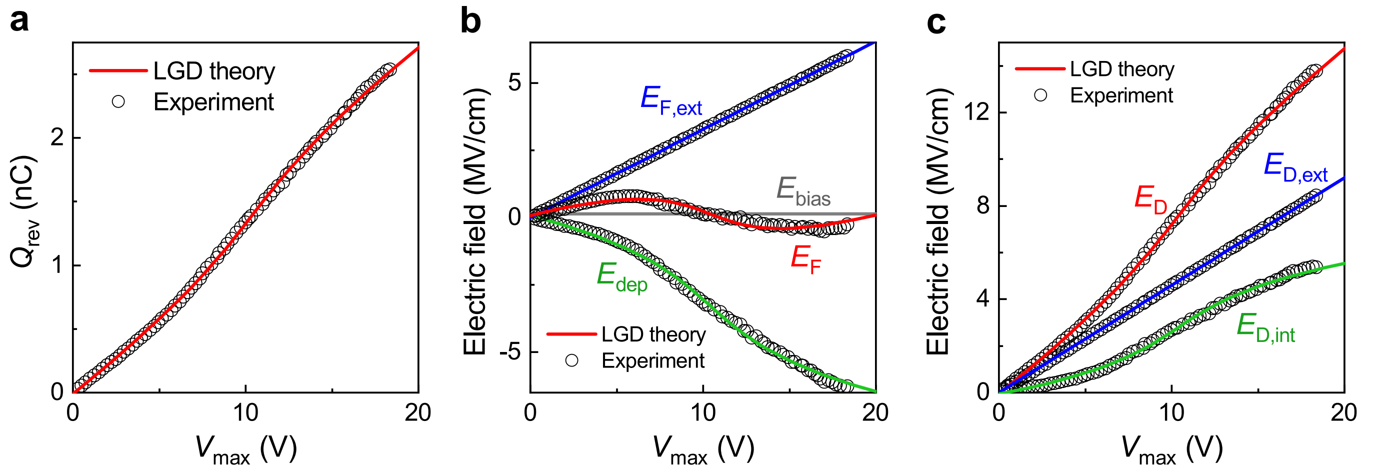


**Extended Data Fig. 5 | Comparison of theory and experiment of pulsed charge–voltage measurements on TiN/HZO/$Ta_2O_5$/TiN samples.** **a**, Reversibly stored charge $Q_{rev}$ as a function of maximum voltage across the capacitor $V_{max}$ as shown in Fig. 3g; solid lines correspond to theoretical calculations using Landau–Ginzburg–Devonshire (LGD) theory. **b**, Calculated electric field contributions in the ferroelectric layer as a function of $V_{max}$. See main text and Supplementary Information for details of nomenclature. **c**, Calculated electric field contributions in the dielectric layer as a function of $V_{max}$. See main text and Supplementary Information for details of nomenclature.


Provided by Sächsische Landesbibliothek - Staats- und Universitätsbibliothek Dresden

Final edited form was published in "Nature". 2019, 565, S. 464-467. ISSN 1476-4687.
https://doi.org/10.1038/s41586-018-0854-z

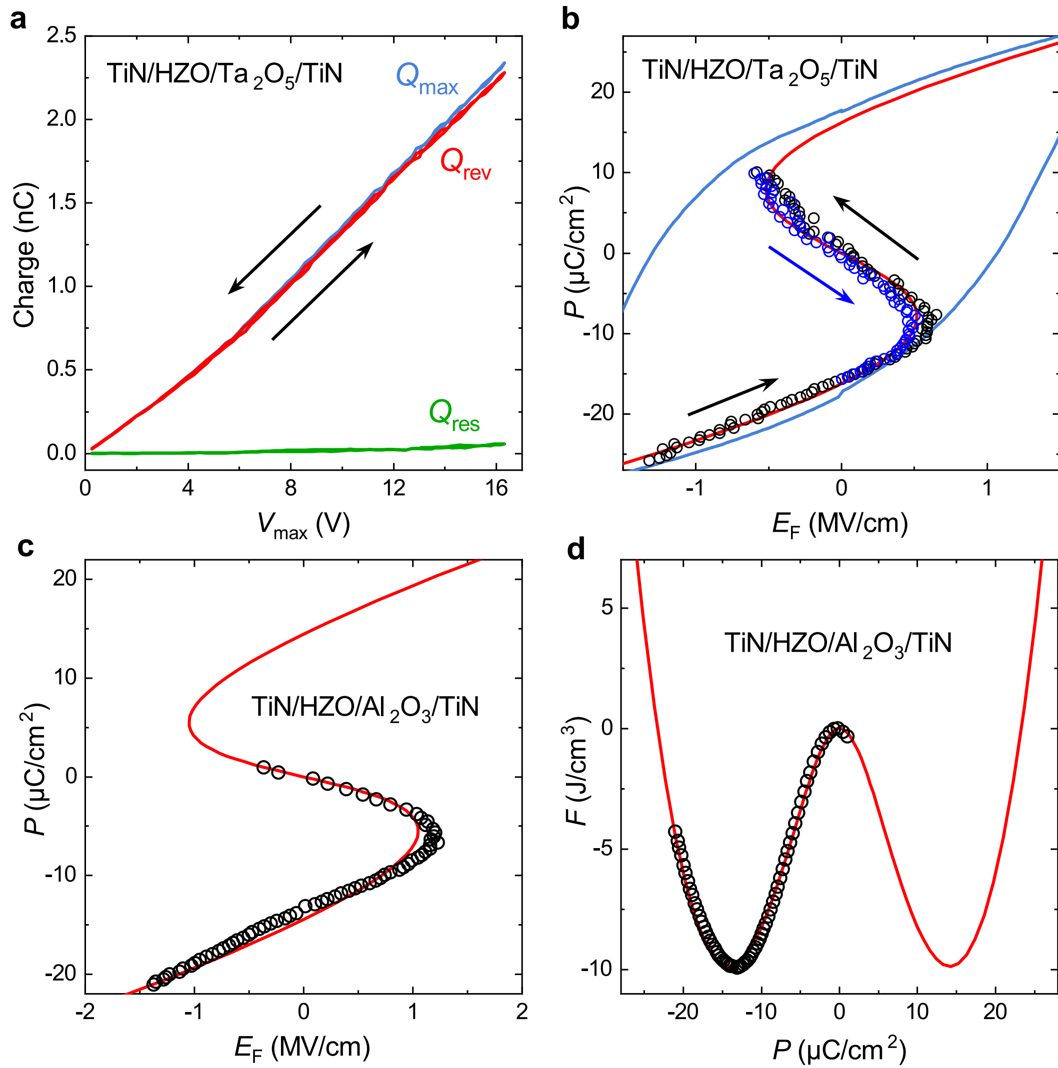


**Extended Data Fig. 6 | Confirmation of hysteresis-free operation and negative capacitance in TiN/HZO/Al$_2$O$_3$/TiN samples. a**, Pulsed charge–voltage hysteresis measurement of a TiN/HZO/Ta$_2$O$_5$/TiN capacitor. See main text for details of nomenclature. Black arrows indicate sweep directions of increasing and decreasing $V_{max}$. **b**, 'S'-shaped $P$–$E_F$ curve calculated from the data in **a** as described in Supplementary Information. Black data points and arrows correspond to the increasing $V_{max}$ sweep direction, while blue data points and arrows indicate the decreasing $V_{max}$ sweep direction. The red line corresponds to LGD theory, and the blue line shows the $P$–$E_F$ hysteresis measured on a TiN/HZO/TiN sample. **c**, 'S'-shaped $P$–$E_F$ curve calculated from pulsed charge–voltage measurements (data points) of a TiN/HZO/Al$_2$O$_3$/TiN capacitor. The red line shows LGD theory calculations. **d**, Integrating the $P$–$E_F$ characteristics in **c** results in a double-well energy landscape (red curve shows LGD theory) from experimental data (data points).


Provided by Sächsische Landesbibliothek - Staats- und Universitätsbibliothek Dresden

Final edited form was published in "Nature". 2019, 565, S. 464-467. ISSN 1476-4687.
https://doi.org/10.1038/s41586-018-0854-z

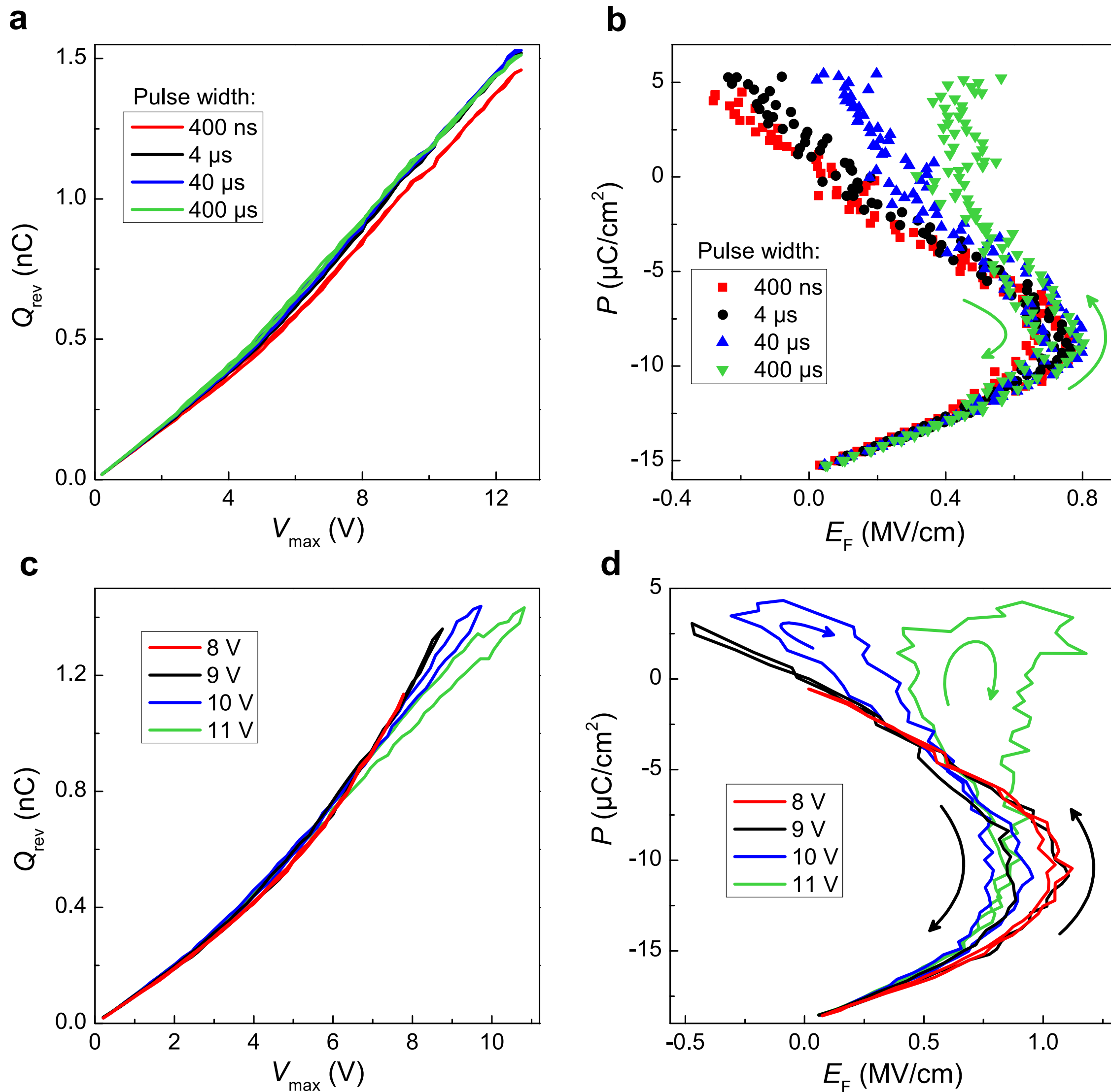


**Extended Data Fig. 7 | Investigation of the transition from hysteresis-free negative capacitance to hysteretic switching.** **a**, Pulsed charge–voltage hysteresis measurement of a TiN/HZO/$Ta_2O_5$/TiN capacitor (same as in Fig. 3) for different pulse widths (see key). **b**, $P$–$E_F$ curves calculated from the data in **a**. Green arrows indicate hysteresis when applying first increasing and then decreasing voltage pulses $V_{max}$. **c**, Pulsed charge–voltage hysteresis measurement of a TiN/HZO/$Al_2O_3$/TiN capacitor with 3-nm $Al_2O_3$ for successively increasing maximum pulse voltages (see key). **d**, $P$–$E_F$ curves calculated from the data in **c**. Arrows indicate hysteresis when applying first increasing and then decreasing voltage pulses $V_{max}$. Clockwise hysteresis is caused by charge-trapping.


Provided by Sächsische Landesbibliothek - Staats- und Universitätsbibliothek Dresden